University of Cape Town

Honours Thesis

Measurements of dimuon resonances and the non-prompt J/ψ production fraction in pp collisions at ATLAS at $\sqrt{s} = 13$ TeV

Author:
Lara Mason

Supervisor:
Dr. Andrew Hamilton

A thesis submitted in fulfilment of the requirements for the degree of Bachelor of Science (Honours)

in the

UCT-ATLAS Group,
Department of Physics

October 2015

Declaration of Authorship

I, Lara Mason, declare that this thesis titled 'Measurements of dimuon resonances and the non-prompt J/ψ production fraction in pp collisions at ATLAS at $\sqrt{s} = 13$ TeV' and the work presented in it are my own.

The data used in this thesis were taken by the ATLAS Collaboration at the LHC at CERN, Geneva. The analysis produced for this paper represents the final stage of a long process of detector design, detector construction, data collection, event reconstruction, data validation and calibration. The large volume of work that went into the production of the data deserves the majority of the credit for the results that are presented. My contribution to this work was the final evaluation of the reconstructed data into the physics conclusions drawn. The plots presented are my own work, unless otherwise stated. The results have been reviewed by the South African National Contact Physicist in ATLAS.

Signed: ______________________

Date: ______________________

University of Cape Town

Abstract

Faculty of Science
Department of Physics

Bachelor of Science (Honours)

Measurements of dimuon resonances and the non-prompt J/ψ production fraction in pp collisions at ATLAS at $\sqrt{s} = 13$ TeV

by Lara Mason

A study of the dimuon spectrum at ATLAS is done using early $\sqrt{s} = 13$ TeV data. The Z boson, J/ψ, $\psi(2S)$ and Υ(1S) are identified and found to have masses of (90.92 $\pm$ 0.09) GeV, (3094.5 $\pm$ 0.5) MeV, (3689 $\pm$ 4) MeV and (9454 $\pm$ 18) MeV. The production models of the J/ψ are examined, and a fit to the pseudo-proper time of the J/ψ decay is used to distinguish the prompt from the non-prompt production modes. The non-prompt production fraction of J/ψ is studied as a function of p_T using a total integrated luminosity of (3.6 $\pm$ 0.2) pb^{-1}. The non-prompt production fraction is found to increase with increasing p_T of the dimuon system, in agreement with previous measurements and theoretical predictions.

Acknowledgements

The first and largest thanks goes to my supervisor, Dr. Andrew Hamilton. Thank you for your patience, enthusiasm, support, and eternal optimism in my abilities, and for always having the time to sit down and chat to me. Thank you for letting me follow you around CERN, and for casually suggesting I try to reproduce the dimuon spectrum plot we saw in a presentation there, which led to this topic. In the midst of all the chaos, you still had time to train for a marathon with me - I feel there is some symbolism there. In short, thank you for everything. I couldn't have wished for a better supervisor.

A huge thank you to everyone at ATLAS who contributed to producing the data that made this analysis possible, and to everyone who helped me with trying to make ROOT do what I wanted it to do.

Thank you to my dad for being an endless source of physics articles, books, and jokes, and for always taking an interest in what I love. To the rest of my family, who have no idea what I do, but support me in it anyway.

And to my office-mates, for getting me through this year.

Contents

Chapter 1

Theory (The Standard Model)

The aim of particle physics is to understand and describe all matter that makes up our universe, as well as the interactions that occur via the fundamental forces of nature. The dominant mathematical framework that currently underlies particle physics is the Standard Model, which successfully describes all particles discovered thus far. The SM is a quantum field theory which incorporates quantum mechanics and relativity in the description of fundamental particles and their interactions, including three of the four fundamental forces; the strong, weak and electromagnetic forces. Forces are mediated by the exchange between fermions of a spin 1 vector boson. The Standard Model Lagrangian $\mathcal{L}$ is symmetric under local $SU(3)_C \otimes SU(2)_L \otimes U(1)_Y$ transformations, the dynamics implied by which are called Quantum Chromodynamics ($SU(3)_C$) and GSW Electroweak Theory ($SU(2)_L \otimes U(1)_Y$). The fourth fundamental force, gravity, is not part of the Standard Model and is described by General Relativity, which is not a quantum field theory.

The material for the following theory section comes predominantly from [1], [2]. The five bosons predicted by the Standard Model are described in Table 1.1, with the masses given by the Particle Data Group [3]. There are four elementary vector bosons (γ, g, Z, $\mathrm{W}^{+/-}$), which mediate force, and one elementary scalar boson, the Higgs, which provides the mechanism by which particles, in particular the two mediators of the weak force (the $\mathrm{W}^{\pm}$ and Z bosons), acquire mass. However, simply adding mass terms for these particles to the SM Lagrangian would violate the local gauge invariance. In order to generate these masses, then, a scalar potential is introduced with a minimum along a circle in the complex plane. In order to investigate the behaviour of this field at its minimum, a point on the circle must be chosen, and hence the symmetry governing the dynamics of the field is no longer present. This is spontaneous symmetry breaking [4]. Discovered at the LHC at CERN in 2012 [5] [6], the Higgs was the final particle predicted by the SM that had yet to be discovered, and signified an important validation of the theory.

TABLE 1.1: Bosons in the Standard Model

Boson	Mass	Elec. Charge	Spin	Force mediated
photon (γ)	0	0	1	Electromagnetic
Z	(91.1876 $\pm$ 0.0021) GeV	0	1	Weak
W$^{\pm}$	(80.385 $\pm$ 0.015) GeV	$\pm$1	1	Weak
gluon (g)	0	0	1	Strong
Higgs (H)	(125.7 $\pm$ 0.4) GeV	0	0	-

Matter is made up of fermions; particles with spin $\frac{1}{2}$, each with a corresponding antiparticle. All matter particles carry the weak charge and so can interact via the weak force. There are two types of elementary fermions; leptons and quarks. Leptons carry integer units of electric charge, measured in units of $e = 1.602 \times 10^{-19}$ C, while quarks carry fractional electric charges. There are 12 types of leptons, which can be electrically and weakly charged; the electron e and its corresponding neutrino ν_e, the muon μ and its corresponding neutrino ν_μ, and the tau τ and its corresponding neutrino ν_τ, as well as the six antileptons. The antileptons, $\bar{l}$, have opposite quantum numbers to their lepton counterparts. Similarly, there are 12 flavours of quarks, which are electrically, weakly and strongly charged; up (u), down (d), strange (s), charm (c), bottom (b) and top (t), and their six corresponding antiquarks (denoted by $\bar{q}$). Quarks also carry one of three colours, red, green or blue, which are the 'charges' of the strong interaction.

Fermions are divided into three generations, as described in Table 1.2. The electron e, the electron neutrino ν_e, the up quark u and the down quark d form the first generation. The second and third generations comprise heavier copies of the first generation particles, while possessing the same fundamental properties as their first-generation counterparts.

Hadrons are particles that are composed of quarks, antiquarks and gluons. They fall into two categories; mesons, composed of a quark and an antiquark, and baryons, composed of three quarks. In this paper the J/ψ and Υ mesons and their excited states will be discussed, as well as the Z boson.

Table 1.2: Fermions in the Standard Model

	Fermion	Generation	Charge	Mass (MeV)
Quarks	u	I	$+\frac{2}{3}$	$(2.3\ ^{+0.7}_{-0.5})$
	c	II		(1275 ± 25)
	t	III		(173030 ± 520)
	d	I	$-\frac{1}{3}$	$(4.8\ ^{+0.5}_{-0.3})$
	s	II		(95 ± 5)
	b	III		(4180 ± 30)
Leptons	e	I	-1	$(0.510998928 \pm 0.000000011)$
	μ	II		$(105.6583715 \pm 0.0000035)$
	τ	III		(1776.82 ± 0.16)
	ν_e	I	0	$< 2 \times 10^{-6}$
	ν_μ	II		$< 2 \times 10^{-6}$
	τ	III		$< 2 \times 10^{-6}$

1.1 Electroweak Interactions

Quantum Electrodynamics (QED) is the quantum field theory describing electromagnetism. The electromagnetic force is mediated by the photon (γ) as described in Table 1.1, which is transmitted between electrically charged particles. The following QED (and QCD) sections are largely derived from [2]. The Feynman rules are derived from the Dirac equation,

$$(i\gamma^\mu \partial_\mu - m)\psi(x) = 0, \tag{1.1}$$

where γ_μ represents the Dirac matrices. There are four plane wave solutions to the Dirac equation - two particle solutions and two antiparticle solutions. The interactions of spin $\frac{1}{2}$ particles, denoted ψ, are given by the Dirac Lagrangian, which is required to preserve its form under Lorentz transformations. In order to make the Lagrangian Lorentz-invariant, we define

$$\bar{\psi} = \psi^\dagger \gamma^0, \tag{1.2}$$

so that $\bar{\psi}\psi$ is a Lorentz scalar and $\bar{\psi}\gamma^\mu\psi$ is a Lorentz vector. The Dirac Lagrangian is therefore

$$\mathcal{L}_{Dirac} = \bar{\psi}(i\gamma^\mu \partial_\mu - m)\psi, \tag{1.3}$$

and is indeed Lorentz-invariant, since in a global phase transformation, $\bar{\psi} \to e^{-i\theta}\bar{\psi}$. However, performing a local gauge transformation of the form

$$\psi(x) \to e^{i\alpha(x)}\psi(x), \tag{1.4}$$

the Lagrangian transforms as

$$\mathcal{L} \to \mathcal{L} - (\partial_\mu \theta)\bar{\psi}\gamma^\mu\psi. \tag{1.5}$$

The Lagrangian of a gauge theory must be invariant under local transformations of the form (1.4), since gauge theories underlie the connection between particles and their interactions. It is therefore a crucial property of the QED Lagrangian that it is gauge-invariant, and so it is necessary to introduce the massless vector field A_μ, which transforms as

$$A_\mu(x) \to A_\mu(x) + \partial_\mu \theta(x). \tag{1.6}$$

The electromagnetic field strength tensor is defined as $F_{\mu\nu} = \partial_\mu A_\nu - \partial_\nu A_\mu$. Defining the gauge covariant derivative

$$D_\mu = \partial_\mu + ieA_\mu(x), \tag{1.7}$$

the QED Lagrangian is then

$$\mathcal{L}_{QED} = \bar{\psi}(i\gamma^\mu D_\mu - m)\psi - \frac{1}{4}F_{\mu\nu}F^{\mu\nu}. \tag{1.8}$$

The unification of the electromagnetic and weak interactions occurs at energies on the order of 100 GeV, leading to the GSW Theory of Electroweak Interactions. As described in Table 1.1, the weak force is mediated by $W^\pm$ and Z bosons. The charge of the weak interaction is weak isospin, described by the gauge group $SU(2)_L$. All fermions carry it, and hence can undergo weak interactions. The W boson couples pairs of quarks which differ by one unit of electric charge, e, or it couples a lepton l to its corresponding neutrino ν_l. In the case of quarks, the coupling strength between quarks of the same generation is greatest. The weak interaction is the only known interaction in which the flavours of the incoming and outgoing fermions can be different. In order to couple the weak and EM forces, GSW models the gauge group of electroweak interactions as the product of two groups, $SU(2) \otimes U(1)_Y$, where the Y stands for hypercharge.

1.2 QCD

The strong interaction, mediated by the gluon, is described by Quantum Chromodynamics. The 'charge' of the strong force is colour, and is carried by quarks and gluons. Single quarks do not exist in nature due to asymptotic freedom, a feature of QCD, whereby the magnitude of the strong force increases with distance. As two quarks are "pulled apart", pair production becomes energetically favourable when the quarks are a distance $\sim 10^{-15}$m apart, and a $q\bar{q}$ pair is produced. Instead of isolating the quarks, then, the produced quarks combine with the "separated" quarks, leading to the production of hadrons. This is the underlying theory of the production of jets.

A $q\bar{q}$ state can occur in one of 9 colour combinations, as shown by the colour octet and colour singlet on the RHS of Figure 1.1. A colourless $q\bar{q}$ particle is one which is in a colour singlet state, which is mathematically analogous to a spin singlet state and is represented by

$$(r\bar{r} + b\bar{b} + g\bar{g})/\sqrt{3}. \tag{1.9}$$

The colour confinement hypothesis states that only colour singlet states can occur as free particles [7], and hence (1.9) is the colour wavefunction for all mesons, with the $q\bar{q}$ effectively cancelling each other's charge. For a baryon to exist, each quark must have a different colour so that the qqq state is colour neutral (an analogy to optical theory, where red + blue + green = white). A more exotic particle, the pentaquark, was recently discovered at CERN [8], with a colour-anticolour pair and three quarks of colour red, green and blue.

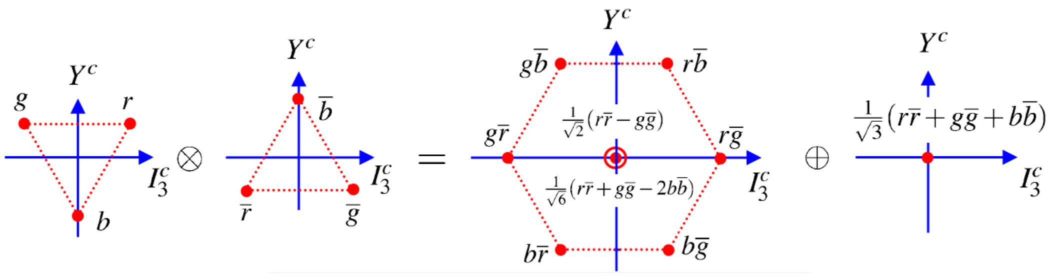

FIGURE 1.1: The combination of colour with anticolour in determining the $q\bar{q}$ state is mathematically identical to the construction of meson wavefunctions with uds flavour symmetry. I_3^C (colour isospin) and Y^c (colour hypercharge) are the two quantum numbers of the colour states. This diagram represents the convolution of the colour quantum numbers of a quark and antiquark (LHS) giving 9 possible $q\bar{q}$ states.

Determining the wavefunction of a gluon is a slightly more complicated case than determining that of a meson. Unlike the neutral photon, the mediator of QED, the gluon itself carries colour and anticolour. Because they are charged (in the sense of QCD), gluons interact strongly with quarks and with each other. This interaction limits the distance over which the gluons can travel, confining the range of the strong force. However, if we were to have a gluon in a colour singlet state, it would be unconfined and would behave like a strongly interacting photon, leading to infinite range strong force. Hence we predict only 8 physical gluons, each in some combination of colour and anticolour [7]. In the context of gauge field theory, this is supported due to the strong interaction arising from a fundamental SU(3) symmetry, as the strong interaction is invariant under rotations in colour space. The generators of this symmetry group are the 8 Gell-Mann matrices, and hence we would predict 8 gluons.

The starting point for the QCD Lagrangian is once again the Dirac Lagrangian, where the ψ now represents the quarks, which have mass. We perform a local gauge transformation, which now takes the form

$$\psi \to e^{i\phi} e^{-ig\boldsymbol{\lambda}\cdot\psi}\psi, \tag{1.10}$$

where λ represents the eight 3x3 Gell-Mann matrices. These form a group known as the $SU(3)_C$ group. $\phi = -\boldsymbol{a}/g$ is a vector, with **a** representing 8 real numbers and g the strong coupling constant. We introduce once again the covariant derivative

$$D_\mu = \partial_\mu + ig\boldsymbol{\lambda}\cdot\boldsymbol{G_\mu}, \tag{1.11}$$

where $\boldsymbol{G_\mu}$ represents the fields of the eight gluons, carrying the various combinations of colour and anticolour. The final gauge-invariant form of the QCD Lagrangian is then given by

$$\mathcal{L}_{QCD} = \bar{\psi}^j(i\gamma^\mu D_\mu^{jk} - m^{jk})\psi^k - \frac{1}{4}F^\alpha_{\mu\nu}F^{\mu\nu}_\alpha, \tag{1.12}$$

where the indices j, k run over the number of quarks [9].

1.3 Kinematics of proton-proton collisions

A proton consists of three valence quarks (uud), which determine the quantum numbers of the proton. The valence quarks can self-interact via gluons, which can themselves self-interact in order to form further $q\bar{q}$ pairs within the proton. These additional quarks are known as sea quarks, and spontaneously appear and disappear from existence. These quarks and gluons, collectively termed partons, are described by universal parton distribution functions (PDFs), on which the structure of the proton depends. At high collision energies (examined in this paper), the partons are effectively free to interact, each with a fraction of the proton's total momentum. The PDFs can be used to predict the rates of scattering processes [10].

The energy, momentum and mass (invariant under a change of reference frame) of a particle are related by $p^\mu p_\mu = E^2 - \mathbf{p}^2 = m^2$. The centre of mass energy of a collision is denoted $\sqrt{s}$, as the Lorentz invariant quantity s for a two particle collision is given by

$$s = \left(\sum_{i=1}^{2} E_i\right)^2 - \left(\sum_{i=1}^{2} \mathbf{p}_i\right)^2. \tag{1.13}$$

At the LHC, pp collisions are currently running at $\sqrt{s} = 13$ TeV, while the partons interact with a fractional energy, denoted $\hat{s}$.

Chapter 2

CERN, the LHC, and ATLAS

The Large Hadron Collider (LHC) is a particle accelerator located at CERN (Conseil Européen pour la Recherche Nucléaire, or European Organisation for Nuclear Research) in Geneva, Switzerland. With a circumference of 26.7km and being located approximately 100m below ground, the LHC facilitates proton-proton collisions which allow its associated experiments to perform precision measurements of the Standard Model, and to search for physics beyond it. There are four main experiments located around the LHC ring; ATLAS, ALICE, CMS and LHCb. This paper will study data collected at the ATLAS experiment.

Protons are stable particles, and thus can be used to make up the LHC beam. If the energy ($\hat{s}$) at which the partons interact corresponds to a resonance of a certain particle, that particle may be produced and will then subsequently decay. Particles with a very short lifetime (smaller than approximately 10^{-10} s) decay before they can pass through the detector, and thus can only be identified by their decay products. Unstable particles with longer lifetimes, such as the muon, can propagate over several meters before decaying and thus can pass through the detector. In this paper, the dimuon invariant mass is used to detect the presence of the J/ψ, $\psi(2S)$, Υ and Z, all of which can be produced in a pp collision but can subsequently decay to $\mu^+\mu^-$.

The LHC is the last of a system of progressively larger and more powerful accelerators at CERN, which make use of the proton's electric charge in using electric and magnetic fields to accelerate and steer the protons. The protons are collected into compact clusters called bunches, which are spread around the circumference of the ring. The super-conducting magnet system within the tunnel accelerates, steers, and focuses the two proton beams, made up of these bunches, travelling in opposite directions around the ring. At present, the LHC is running at a centre of mass energy $\sqrt{s} = 13$ TeV, a lower energy than its design $\sqrt{s} = 14$ TeV.

In December 2012 the LHC ended its three year long Run I, culminating in a collision energy of 8 TeV with a luminosity of approximately 25 fb^{-1}. The collider underwent nearly two years of maintenance and upgrading (termed the Long Shutdown) before restarting in early 2015 with a significantly higher collision energy of 13 TeV.

2.1 The ATLAS (A Toroidal LHC ApparatuS) Detector

The ATLAS detector [11] consists of multiple layers of concentric subdetectors, each of which has been designed to track and measure the energy and/or momenta of particles passing through it. The detector comprises the Inner Detector, two calorimeters, and the Muon Spectrometer. The Inner Detector tracks the particles, the calorimeters measure their energy, and the Muon Spectrometer detects the particles (muons) which make it through the calorimeter. The components of the detector are depicted in Figure 2.1.

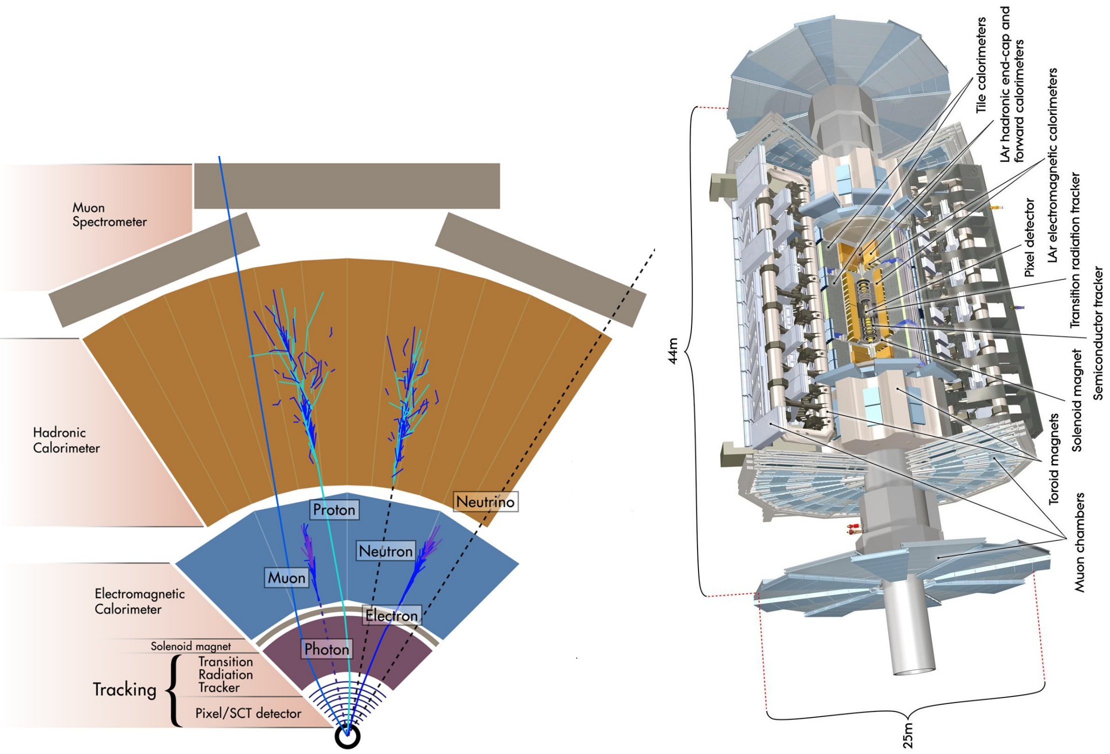

FIGURE 2.1: A slice of the ATLAS detector showing how and where various particles are detected (left) and a cartoon depiction of the full detector setup (right) [12].

The nominal proton-proton collision point serves as the origin of the coordinate system used at ATLAS. The beam-line defines the z-direction, while the x-y plane lies perpendicular to the beam, with the positive x-axis pointing to the centre of the LHC ring, and the positive y-axis pointing vertically upwards. The azimuthal angle, ϕ, lies in the x-y plane, and the polar angle θ is measured from the z-axis. Transverse energy of a particle is defined as

$$E_T = E \cdot \sin\theta. \tag{2.1}$$

It is common to define the pseudorapidity,

$$\eta = -\ln\left[\tan\left(\frac{\theta}{2}\right)\right], \tag{2.2}$$

to be used in the place of θ. $\eta = 0$ points vertically upwards, and runs to $\eta = \infty$ at the beam line. The detector is largely symmetric about $\eta = 0$. The pseudorapidity corresponds to the rapidity y in the limit of ultrarelativistic motion, with

$$y = \frac{1}{2}\ln\frac{E + p_z}{E - p_z}. \tag{2.3}$$

2.1.1 Inner Detector

The Inner Detector encompasses three subdetectors; the Silicone Pixels and the Semi-Conductor Tracker, which cover $|\eta| < 2.5$, and the Transition Radiation Tracker, with an $|\eta|$ coverage of up to 2. It is submerged in a 2T field along the z-axis, created by a solenoid, which bends the charged particles and facilitates measurement of their charge and momentum. The Pixel Detector reconstructs charged particle tracks for primary vertex reconstruction. During the long shutdown, a fourth layer (the Insertable B-Layer) was added to the Pixel Detector, to further improve the accuracy of reconstruction of primary and secondary vertices, in which the Pixel Detector plays a key role. This reconstruction of charged particle tracks is essential for the the detection of long-lived particles such as those containing b quarks, which form part of the J/ψ analysis performed in this paper. The Semi-Conductor Tracker, comprising several layers of silicone microstrips, provides important information for high-precision vertex position and particle momentum measurements. The material of the TRT, the third subdetector, is ionised as charged particles pass through it. The amount of transition radiation emitted is specific to each particle.

2.1.2 Calorimeters

The ATLAS calorimeter system is made up of the hadronic and the electromagnetic calorimeters, which encircle the Inner Detector, and performs the energy measurement of most of the particles created in a collision. The electromagnetic (EM) calorimeter allows for precise measurements of electron, positron, and photon energies. The hadronic calorimeter surrounds the EM calorimeter, and measures the energy of hadronically interacting particles. The calorimeter system also includes the forward calorimeter (FCal) which measures the particles with a much higher η.

The electromagnetic calorimeter, made of layers of liquid argon and lead absorbers, consists of a barrel part and two endcaps, and covers the detector up to a pseudorapidity $|\eta| = 3.2$. As the charged particles move through the calorimeter material they generate an EM shower, which ionizes the liquid argon. The ionization electrons then drift towards the electrodes, which collect the charge. The hadronic calorimeter, also consisting of a barrel and endcaps and covering the same pseudorapidity range as the EM calorimeter, is made up of tiles of plastic scintillator and LAr cells which sample hadronic shower energy using signals from particles, which are amplified using photomultiplier tubes.

2.1.3 Muon Spectrometer

The muon subdetectors which make up the Muon Spectrometer are the outermost layers of the ATLAS detector, and are designed to measure the momentum of muons which pass through the Inner Detector and calorimeters without depositing all of their energy therein. The muon system, consisting of a barrel ($|\eta| < 1.05$) and two endcap sections, has a system of superconducting air-core toroidal magnets. The muons, being electromagnetically charged, bend in this magnetic field, allowing the subdetectors to make measurements of the muon's transverse momentum. The subdetectors are the Monitored Drift Tubes, the Cathode Strip Chamber, the Resistive Plate Chambers and the Thin Gap Chambers, collectively covering a pseudorapidity $|\eta| < 2.7$. Combined with identifications made by the Inner Detector, the Muon Spectrometer identifies muon track candidates, and is designed to provide momentum measurements with a resolution better than 3% [13].

Precision measurements in η are performed by the Monitored Drift Tubes, which form the principal component of the MS system [14]. The MDT's cover a region of $|\eta| < 1.0$ in the barrel, and $1.0 < |\eta| < 2.7$ in the endcaps. The tubes are filled with a gas mixture and a central anode wire carrying a certain potential. As a charged particle (hereafter referred to as a muon) passes through the gas, it ionises and creates an avalanche of electron-ion pairs which accelerate towards the anode under the high voltage, creating a measurable signal. The muon track can thus be reconstructed. In the very forward region, with $|\eta| > 2$, CSCs are used in place of MDTs in order to track the bending of the muon in the toroidal field by employing a similar method to the MDTs.

Muon triggering capabilities are provided by the Resistive Plate Chambers and the Thin Gap Chambers, which choose what collisions are interesting enough to be saved for further analysis. The RPSs and TGCs also provide (η, ϕ) position measurements with a typical spatial resolution of 5–10 mm [13]. The muon trigger must be able to estimate the momentum of a muon passing through the MS in fractions of a nanosecond, and must associate a track with a particular bunch crossing. This requires fast signal generation, with timing resolution better than the bunch-crossing interval [14]. The RPC are used for triggering in the barrel, and the TGC in the endcaps. There are four different types of muons that can be identified, which differ according to where and how they are detected. This is discussed in the Muon Reconstruction Performance Section below.

Prior to commencement of Run 2 at the LHC, the final missing chambers were added to the transition region between the barrel and the endcaps, completing the MS to its original design. Four MDT chambers equipped with RPC were also installed in that region, in order to improve efficiency [13].

2.1.4 Trigger

The LHC has a high collision rate and large production cross section, and so the rate of particle collisions is immense. At the optimum luminosity and bunch spacing, collisions occur at a rate of 40 MHz, while ATLAS is capable of recording events for further analysis at a rate of only 400 Hz (0.0004 MHz) due to processing and storage constraints. For this reason, ATLAS employs a sophisticated three-level trigger and data acquisition system (TDAQ) in order to select events whose signature displays interesting physics and ignore uninteresting ones. This selection is made in microseconds.

The hardware-based level-1 trigger uses information from the calorimeters to form regions of interest and make cuts on objects such as jets and muons, deciding whether to save the event. Information about the regions of interest are then passed on to the software-based level-2 trigger, which again determines whether the event is physically interesting. The final step in the trigger system is the event filter, which uses algorithms to detect objects such as electrons, muons, jets, photons and missing transverse energy, and separate them into analysis streams. The event filter and level-2 trigger are collectively known as the high-level trigger. Events must be selected by at least one trigger in order to be saved for further analysis.

2.2 Muon Reconstruction Performance

The reconstruction and identification by the ATLAS detector of muons is of particular importance for this analysis, which uses a dimuon signal. Muons are detected in a variety of ways, and are categorised according to the level of certainty in their detection. Information from the Inner Detector and Muon Spectrometer (and, to a lesser extent, the calorimeters) is used to identify muon candidates and reconstruct their trajectory and momentum. A muon leaves a curved track in the Inner Detector, a small energy deposit in the calorimeters, and a curved track in the Muon Spectrometer. There are four types of muons; Combined, Stand-Alone, Calorimeter-tagged and Segment-tagged.

Combined muons, whose tracks are reconstructed independently in both the Inner Detector and the Muon Spectrometer, are the main type of muon used at ATLAS, as they provide the highest quality in terms of purity and momentum resolution. Stand-Alone muon tracks are reconstructed only in the Muon Spectrometer, and are used to detect muons in the region $2.5 < |\eta| < 2.7$. A Segment-Tagged muon is a track in the Inner Detector whose extrapolation to the MS is associated with at least one hit in the Monitored Drift Tubes or Cathode Strip Chamber. This is especially applicable to low p_T muons that do not transverse enough precision chambers for a full momentum measurement in the MS. A track in the Inner Detector which corresponds to an energy deposit in the calorimeter compatible with a minimum ionizing particle is used to identify Calorimeter-Tagged muons. This applies mostly to the region of very small η, where the MS is not fully instrumented. These muons are of the lowest purity.

Reconstruction efficiency is measured using a "tag and probe" method at the J/ψ and Z resonances, which allows for a measurement of the efficiency with which the Muon Spectrometer detects a muon. The method selects a "tag": a well reconstructed muon fulfilling tight criteria, as well as a different set of tracks in the Inner Detector corresponding to the same event. The corresponding "probe" is a signal in the MS , found within a cone of size $\Delta R = \sqrt{\Delta\eta^2 + \Delta\phi^2} < 0.05$ around the tag track in the $\eta - \phi$ plane. To measure the reconstruction efficiency via a $Z \rightarrow \mu^+\mu^- (J/\psi \rightarrow \mu^+\mu^-)$, a tag muon with a $p_T \geq 28(4)$ GeV triggers the event readout. The corresponding probe must have $p_T \geq 10(2.5)$ GeV [13]. The efficiencies from data can then be compared to detector simulation efficiencies, and the ratio between between the two (the efficiency scale factor) used to correct simulation. The initial performance of the ATLAS muon reconstruction in Run 2 has been studied and documented using the first 85 pb^{-1} of data, and both the reconstruction and isolation efficiencies have been found to be >99% in most regions of the detector [13].

2.3 Data and Event Selection

The data were accessed in reduced data formats produced by the Muon Performance Group and BPhysics Group. The data formats used in this analysis are xAODs (or, equivalently AODs) and DxAODs. AODs (Analysis Object Data) are a new format, created during the Long Shutdown, which is a summary of the reconstructed event, while DxAODs have further refined content specific to physics and performance groups. Two different skimmed data sets were used in this analysis; the MUON1 and MUON3 versions of the same data. For an event to be recorded in the MUON1 dataset, it is required that there be at least one Combined muon with a $p_T > 24$ GeV and $|\eta| < 2.5$, and a second muon or Inner Detector track with $p_T > 8$ GeV, with a total invariant mass > 60 GeV. For MUON3 we require at least two Combined muons, each with a $p_T > 5$ GeV, and a total invariant mass in (2,4.8) GeV or (7,13) GeV. It is clear, then, that MUON1 is optimized to search for a Z, and MUON 3 to search for Υ or J/ψ.

The ATLAS reconstructed data used in this analysis were collected from early $\sqrt{s} = 13$ TeV collisions at the LHC. The data were collected during Run 267638, which took place on the 13th and 14th of June 2015, during which there were 35,268,547 events recorded. The data sample represents a total integrated luminosity of (3.6 ± 0.2) pb^{-1}. We require that the data pass quality criteria by filtering the luminosity blocks which make up the run through the Good Runs List, which picks out the blocks which were recorded during stable beam operation and with a fully operational detector.

All muon pairs are required to be oppositely charged. J/ψ candidates are selected from pairs where each muon has $|\eta| > 1.3$ and $p_T > 2.5$ GeV, or $|\eta| < 1.3$ and $p_T > 3.5$ GeV. This is in an attempt to discard muons which do not pass fully through the detector, and are therefore not well reconstructed, due to their low energies. A small-η muon is required to have a larger p_T because its momentum will be dominated by the transverse component. A more forward muon, having a larger η, can be high energy without having a large p_T. Υ candidates are selected from muon pairs with each muon having a $p_T > 4$ GeV, and Z candidates are selected from pairs with each muon having a $p_T > 20$ GeV and $|\eta| < 2.47$.

Chapter 3

Z boson

The Z boson is the elementary particle mediating the weak interaction, and appears as a significant bump on the dimuon spectrum. It has a mass of (91.1876 ± 0.0021) GeV [3], is electrically neutral, and has spin 1. The branching fraction Γ_i/Γ of the decay Z$\rightarrow \mu^+\mu^-$ is (3.366 ± 0.007)% [3].

The decay rate of the $Z \rightarrow \mu^+\mu^-$ process is calculable via the Feynman rules. This process is outlined in general in [2], and is depicted in Figure 3.1.

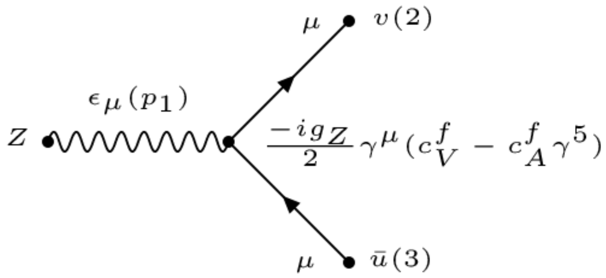

FIGURE 3.1: Labelled Feynman diagram for the dimuon decay of the Z boson.

The decay rate is given by

$$\Gamma = \frac{S|\mathbf{p}|}{8\pi\hbar m_1^2 c}|\mathcal{M}|^2, \tag{3.1}$$

where $|\mathcal{M}|$ denotes the amplitude of the decay, S corrects for overcounting of identical particles in the final state (of which there are none in this calculation), and $\mathbf{p}$ denotes either outgoing momentum in terms of the Z mass, m_Z. The vertex factor for Z, f, f, where f is any fermion, is given as

$$\frac{-ig_Z}{2}\gamma^\mu(c_V^f - c_A^f\gamma^5), \tag{3.2}$$

where g_Z is the neutral coupling constant, and the coefficients c_V^f and c_A^f depend on the particular fermion involved. For muons, $c_V = -\frac{1}{2} + 2\sin^2\theta_w$, and $c_A = -\frac{1}{2}$, where $\theta_W = 28.75°$ is the weak mixing angle. $g_z = \sqrt{4\pi\alpha}/(\sin\theta_W \cos\theta_W)$. There is one weak neutral current running between the two muons, denoted

$$j^\mu = \bar{u}(3)\left(-\frac{ig_Z}{2}\gamma^\mu(c_V^f - c_A^f\gamma^5)\right)v(2). \tag{3.3}$$

The square of the amplitude can then be written

$$|\mathcal{M}|^2 = \left(\frac{g_Z}{2}\right)^2 \epsilon_\mu\epsilon_\nu^* \left(\bar{u}(3)\gamma^\mu(c_V^f - c_A^f\gamma^5)v(2)\right)\left(\bar{v}(2)\gamma^\mu(c_V^{*f} - c_A^{*f}\gamma^5)u(3)\right), \tag{3.4}$$

where * denotes the complex conjugate. Averaging over the three initial polarization states of the Z, using natural units, and taking the masses of the muons to be much less than the mass of the Z, we obtain

$$\langle|\mathcal{M}|^2\rangle = \frac{g_Z^2}{3}(c_V^2 + c_A^2)\left((p_2 \cdot p_3 + \frac{2}{m_Z^2}(p_1 \cdot p_2)(p_1 \cdot p_3)\right). \tag{3.5}$$

Evaluated in the Z rest frame, and setting $\mathbf{p} = \frac{m_Z}{2}$, we obtain

$$\Gamma = \frac{Sm_Z g_Z^2(c_V^2 + c_A^2)}{48\pi}. \tag{3.6}$$

The decay rate of $Z \to \mu^+\mu^-$ is then calculated to be 0.080 GeV. The total decay rate is calculable by summing over all allowed decay modes, with

$$\Gamma_{tot} \sim \sum_f (|c_V^f|^2 + |c_A^f|^2) = 7.3062 \text{ GeV}. \tag{3.7}$$

We can then extract the branching ratio of $Z \to \mu^+\mu^-$ to be 3.337%, with which the PDG value agrees within 1σ.

Observations and measurements of familiar particles, such as the Z boson, are an important verification of the operation of the detector. Z boson production is a standard benchmark process, forming a basis from which reconstruction and trigger efficiencies, detector resolution, and energy scale calibrations can be made. The dimuon decay of the Z boson is easily observable in the dimuon spectrum, as these higher energy events are easily separated from background processes.

3.1 Production

The main process by which Z bosons are produced at the LHC is the Drell-Yan process

$$q\bar{q} \rightarrow Z \rightarrow \mu^{+}\mu^{-}, \tag{3.8}$$

as shown in Figure 3.2(A) and (B) below. Compton scattering and gluon-gluon fusion can also result in the production of a Z, shown in Figure 3.2(C) and (D).

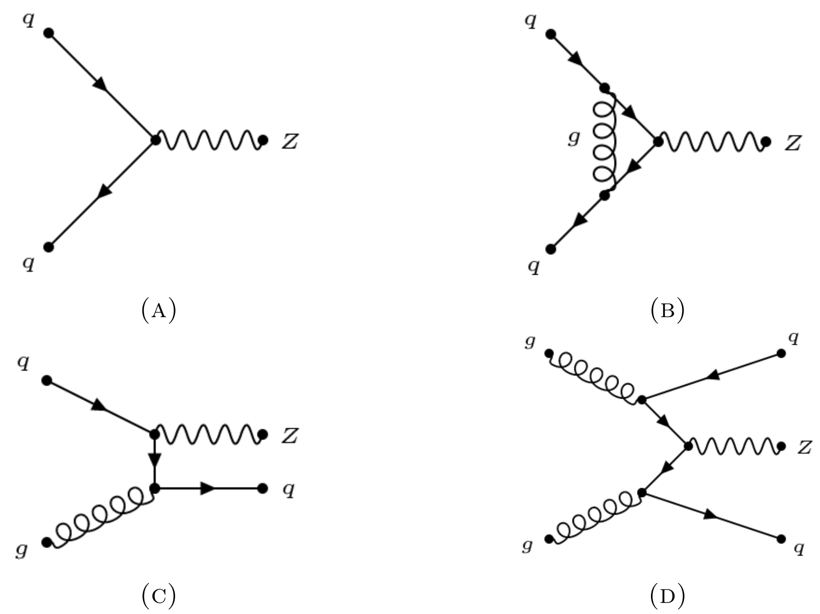

FIGURE 3.2: Sample production modes of the Z boson. Subfigures (A) and (B) show the production of a Z boson via the Drell-Yan process and its higher order correction, (C) shows Compton gluon scattering, and (D) gluon-gluon fusion

3.2 Invariant Mass

A clear peak at the resonance of the Z is visible on the full invariant mass spectrum of $\mu^{+}\mu^{-}$ (see Figure 3.3). Because the cut requiring the invariant mass of the muons in an event be greater than 60 GeV encompasses two or more muons, when examining only dimuon pairs we see invariant masses over the full spectrum. The J/ψ and Z peaks are visible, as is a bump around 60 GeV, which is a result of the invariant mass cut.

Restricting the invariant mass range to that of the Z resonance, and performing a fit of a second degree polynomial to account for background processes combined with a Gaussian distribution, a peak at (90.92 $\pm$ 0.09) GeV was obtained, agreeing with the PDG within

3σ. The uncertainty quoted is statistical, and qiven purely by the fit, which is displayed in Figure 3.4.

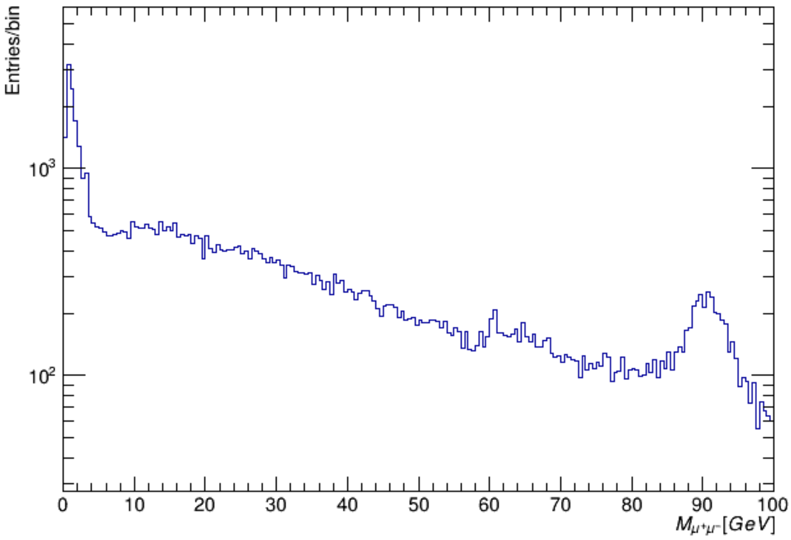

FIGURE 3.3: The invariant mass plot all pairs of oppositely charged muons, using the MUON1 data set

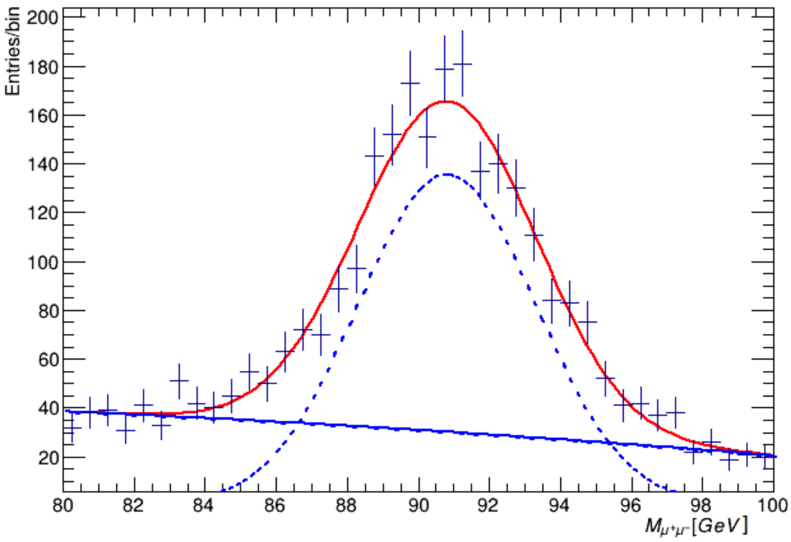

FIGURE 3.4: The dimuon invariant mass plot about the Z boson resonance. The total fit is shown in red, with the background in solid blue and the Gaussian distribution in dashed blue.

Chapter 4

The J/ψ meson

Quarkonium is defined as the bound state of a bottom or charm quark and antiquark. The J/ψ is a 1S bound state of $c\bar{c}$ (charmonium), and was the first of its kind to be found when its discovery was announced simultaneously by two North American groups (working at Brookhaven National Laboratory and the Stanford Linear Accelerator Centre respectively) on November 10 1974 [15] [16]. The announcements featured the observation of a resonance at 3.1 GeV - a considerably more massive particle than anything that had yet been discovered, with a narrow width indicating a life much longer than those particles which decayed strongly. With the group at BNL naming it the J, and the group at SLAC naming it the ψ, the new particle was dubbed the J/ψ. It was a discovery so significant to the world of particle physics that the period has become known as the "November Revolution". The simultaneous discovery is illustrated in Figure 4.1 using plots from the original papers [15] [16].

The J/ψ has a mass of (3096.916 ± 0.011) MeV [3], spin 1 (each constituent quark has a spin of $\frac{1}{2}$) and orbital angular momentum 0. It is electrically neutral, and has both odd charge conjugation and parity ($J^{PC} = 1^{--}$). The branching fraction Γ_i/Γ of the decay $J/\psi \to \mu^+\mu^-$ is (5.93 ± 0.06)% [3]. The mass of the first excited state of the J/ψ, the $\psi(2S)$, is (3686.09 ± 0.04) MeV [3].

The width of the J/ψ meson is narrower than naively expected due to several forbidden or suppressed decay modes. The decay to a D meson ($c\bar{q}$, the lightest meson containing a charm quark), is kinematically blocked since m(J/ψ)< 2m(D). The decay to two gluons, which would then result in a hadronic signature, is blocked by quantum mechanics as it violates charge conjugation parity. Due to the OZI rule, which states that the strong coupling constant must decrease with increasing energy, the decay to three gluons is

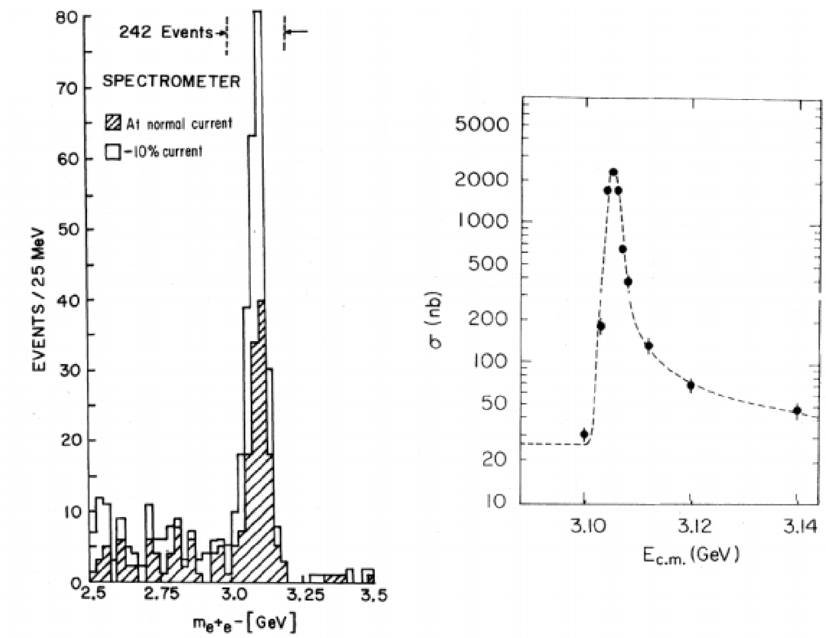

FIGURE 4.1: The discovery of the J/ψ at BNL (left) and SLAC (right)

heavily suppressed [17]. The gluons would be very high energy, and their probability of interaction would hence be low. Because the strong decays of the J/ψ are forbidden or suppressed, the electromagnetic decays can compete, and therefore the decay to two muons (studied in this paper) makes up a large fraction of the J/ψ decay. Electromagnetic decays have a longer Δt and hence a smaller ΔE (due to Heisenberg), leading to a very narrow invariant mass peak.

A spin 0 $c\bar{c}$ state, the η_c meson, also exists, but its strong decays are not blocked. It therefore decays predominantly to hadrons (which become jets) and are not discussed in this analysis.

4.1 Production

Although quarkonium was discovered over 40 years ago, its production in *pp* collisions is not well understood, and there is no model currently proposed which agrees convincingly with experiment on all accounts. It is produced either from QCD sources, labelled prompt production, or via the decay of a *b*-hadron (non-prompt production). The various models describing the production of prompt quarkonium are described below, referring in particular to the J/ψ, although the same models are suggested for the production of the Υ meson, which is to be discussed in the following chapter.

Inclusive production of J/ψ can be due to direct production via parton-parton interactions, or feed-down from higher mass charmonium states such as χ_{c1}, χ_{c2}, or $\psi(2s)$, and is generally a complicated mixture of several processes. In the case of charmonium production, the feed-down contribution from b-hadrons can be experimentally separated from the other production processes. This is due to the long lifetime of the b-hadron. A simple model predicts that the lifetime of the b-hadron, τ_b, is determined solely by the decay of the b quark, which couples predominantly to the c quark via weak decay (the strength of which is described by the CKM matrix element V_{cb}). Thus τ_b is mainly a measurement of $|V_{cb}|$, and is on the order of 1ps [18]. This relatively long lifetime means that the b-hadron travels a short distance (typically on the order of 1mm) in the transverse plane before weakly decaying. Due to the experimental distinguishability of the secondary vertex, we can identify the J/ψs produced from b-hadrons, which are labelled the non-prompt contribution to the production. The remainder is referred to as the prompt contribution.

4.1.1 Prompt Production

There are several models describing prompt J/ψ formation, all of which make predictions for the cross section and angular decay coefficients of the produced charmonium states, but none fully describe all of its known properties. The three models to be discussed are the Colour Evaporation Model, the Colour Singlet Model, and the Colour Octet Model. Each model attempts to factor the production into a relativistic part which describes the production of the quark and antiquark, and a non-relativistic part which describes the bound state $q\bar{q}$. The bound state can be described as such since the mass of the charm quark (1.29 GeV) is much larger than the QCD energy scale ($\Lambda_{QCD} \approx 200$ MeV). The general form of the differential cross section is given by

$$d\sigma(J/\psi + X) = \sum_n \int d\Lambda \frac{d\sigma_{c\bar{c}[n]+X}}{d\Lambda} F_{c\bar{c}[n]}(\Lambda), \tag{4.1}$$

where $d\sigma_{c\bar{c}[n]+X}$ describes the production of the $c\bar{c}$ pair, $F_{c\bar{c}[n]}(\Lambda)$ describes the non-relativistic part of the process, $[n]$ denotes the quantum state of the charmonium, and Λ denotes the energy scale.

The first, the Colour Evaporation Model, is one of the earliest models of quarkonium production. It does not take into account the explicit quantum state of the charmonium, but rather sums over all possible states and corrects by a factor of $\frac{1}{9}$, which is the probability that a $q\bar{q}$ could be in a colour singlet state, as the J/ψ must be. The non-relativistic part of the equation is assumed to be non-zero and constant only in a certain energy scale, and is determined from a fit to the data. The differential cross section is

$$d\sigma(J/\psi + X) = \frac{F_{c\bar{c}[J/\psi]}}{9} \sum_{n} \int d\Lambda \frac{d\sigma_{c\bar{c}[n]+X}}{d\Lambda}. \tag{4.2}$$

While the CEM makes some prediction for the cross section, it makes no prediction about the spin-alignment, and hence is a limited model.

The following two models, the Colour Singlet Model and the Colour Octet Model, both attempt to explicitly take into account the quantum state of the $q\bar{q}$ pair. The Colour Singlet Model (CSM) attempts to describe the hadroproduction of the J/ψ within a perturbative QCD framework, which is problematic due to the fact that quarkonium cannot be formed directly via gluon-gluon fusion [19]. Because the wavefunction of a meson is a colour singlet state, the CSM predicts that the $q\bar{q}$ state must be directly produced in a colur singlet state, possessing the same spin and angular momentum quantum numbers as the quarkonium state into which it will evolve. The probability of this decay is then determined by the wavefunction of the $q\bar{q}$ pair [20]. The differential cross section is given by

$$d\sigma(J/\psi + X) = \int_0^\infty d\Lambda \frac{d\sigma_{c\bar{c}[^3S_1]+X}}{d\Lambda} \psi_{J/\psi}(r = 0). \tag{4.3}$$

The CSM predicts that the J/ψ is formed by the fusion of two gluons as shown in the leading order decay

$$g + g \to c\bar{c} + g, \tag{4.4}$$

[20] with the charmonium being formed in a colour singlet state. The radiation of one gluon is necessary in order to conserve spin. However, this model underestimates the cross section by a factor of 50 and does not adequately describe its shape [21], and also incorrectly predicts that the J/ψ production is dominated by feed-down from χ_c [22]. The CSM has recently been improved by adding higher order contributions [23].

With the introduction of the effective field theory non-relativistic QCD (NRQCD), the alternative to the CSM, the Colour Octet Model, was introduced [21]. The COM does not restrict the initial quarkonium state to being produced in a singlet state, but rather predicts that the J/ψ is produced according to

$$gg \to {}^3P_2^8 \to^3 S_1 + g, \tag{4.5}$$

where the super- and subscript notation ${}^{2S+1}L_J$ indicate spin S and total angular momentum J [17]. Here, the $c\bar{c}$ pair is initially produced in a colour octet state as a χ meson (a p-wave state related to the s-wave state of the J/ψ meson by single photon transitions), which then radiates a gluon and hadronizes into a colour singlet state; the J/ψ. The colour of the $q\bar{q}$ pair is neutralized via the non-perturbative emission of the gluon. The model attempts to formalise the factorisation of relativistic and non-relativistic effects, using the generic expansion for the differential cross section

$$d\sigma(J/\psi + X) = \int_0^{\infty} d\Lambda \frac{d\sigma_{c\bar{c}[n]+X}}{d\Lambda} \langle O_{[n]}{}^{J/\psi} \rangle, \tag{4.6}$$

where the parameters $\langle O_{[n]}{}^{J/\psi} \rangle$ are NRQCD matrix elements associated with the probability of producing a J/ψ from a charmonium in any state $[n]$ through this non-perturbative transmission [24].

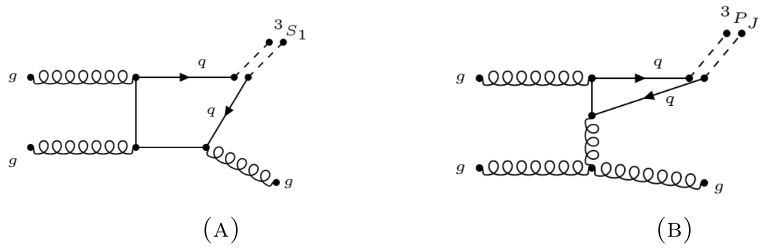

FIGURE 4.2: Possible leading order Feynman diagrams for production of (A)$^3S_1$ (CSM) and (B) $^3P_1$ (COM)

While the cross section predictions of the COM model do agree with experiment, the spin alignment predictions do not match data [21]. There are several other models which attempt to describe the production of the J/ψ, but the COM makes the most promising predictions. Possible Feynmann diagrams for the CSM and COM are depicted in Figure 4.2.

4.1.2 Non-prompt Production

The non-prompt production of J/ψ mesons proceeds via the weak decay of b-hadrons. The measurement of the non-prompt J/ψ cross section comprises three parts; a perturbative QCD prediction of the b quark production, evaluated using Fixed-Order Next-to-Leading-Log (FONLL) calculations (which contain NLO and NNLO QCD considerations), a measurement of the low energy QCD b quark fragmentation into b-hadrons, and an experimental measurement of the b-hadron decay to J/ψ, which is done by measuring the branching fractions [25]. The theoretical prediction of the non-prompt cross-section using FONLL is further described in [26] and [27].

4.2 Invariant Mass

Both the J/ψ and its first excited state, $\psi(2S)$, are clearly present in the dimuon invariant mass spectrum, as plotted in Figure 4.3.

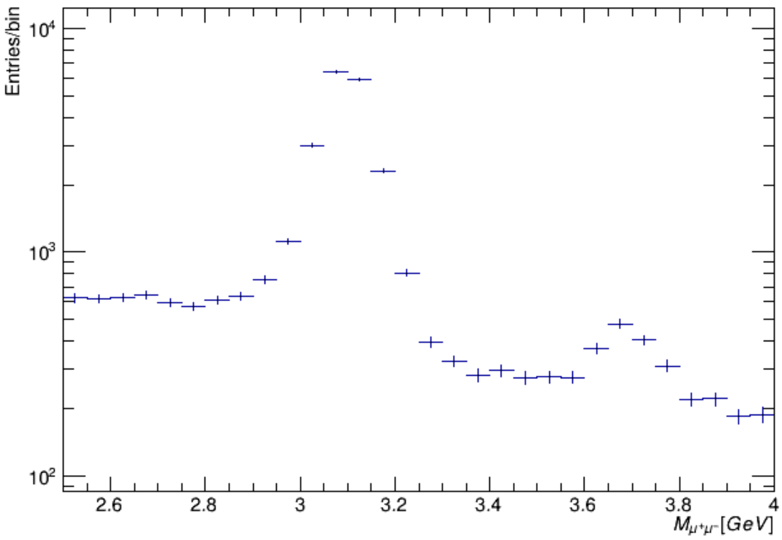

FIGURE 4.3: Logarithmic plot to show the presence of the first excited state of the J/ψ , the $\psi(2S)$, in the dimuon invariant mass spectrum.

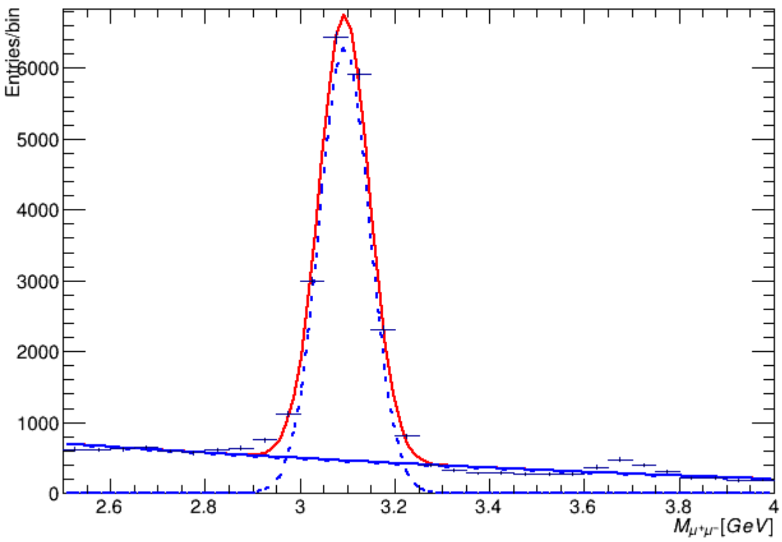

FIGURE 4.4: Dimuon invariant mass plot about the J/ψ resonance with fit results superimposed. The total fit is shown in red, with the background and Gaussian distributions shown in blue.

The data are fit using a second order polynomial to model the background, and a Gaussian distribution to model the signal. The fits presented in Figures 4.4 and 4.5 give

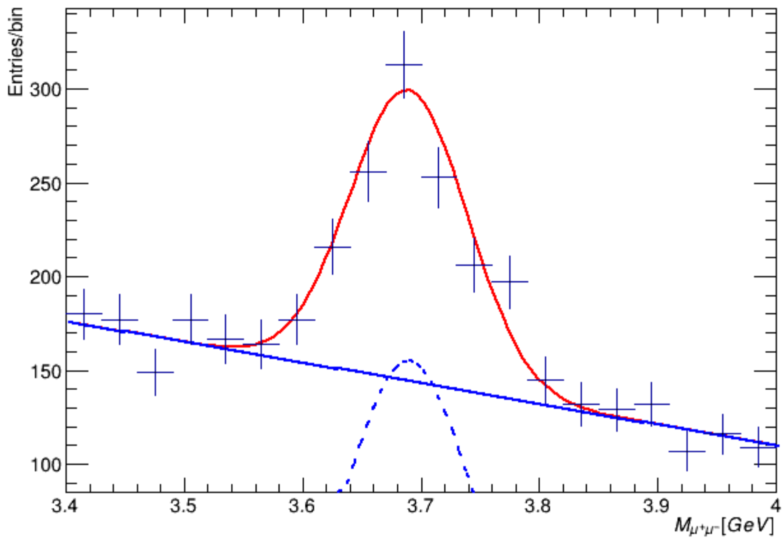

FIGURE 4.5: Dimuon invariant mass plot about the $\psi(2S)$ resonance with fit results superimposed. The total fit is shown in red, with the background and Gaussian distributions shown in blue.

values of (3094.5 ± 0.5) MeV and (3689 ± 4) MeV for the invariant masses of the J/ψ and $\psi(2S)$ mesons respectively. The observed J/ψ invariant mass disagrees with the PDG by 5σ, and that of the $\psi(2S)$ agrees with the PDG within 1σ.

4.3 Non-prompt Production Fraction

While in prompt production the J/ψ decay vertex coincides with the primary proton-proton vertex, in non-prompt production the dimuon vertex is experimentally distinguishable from the primary vertex (see Figure 4.6, where the vertices for a single event have been plotted). One can therefore calculate the fraction of J/ψ decays produced through b-hadron decays to the total number produced:

$$f_b^{J/\psi} = \frac{pp \to b + X \to J/\psi + X'}{pp \xrightarrow{incl.} J/\psi + X''} = \frac{N_{J/\psi}^{non-prompt}}{N_{J/\psi}^{non-prompt} + N_{J/\psi}^{prompt}}. \tag{4.7}$$

4.3.1 Measurement Methodology

The probability that a particle will decay as a function of proper time t follows a decaying exponential distribution $\sim e^{-t/\tau_L}$, with τ_L being the lifetime of the particle. Instead of

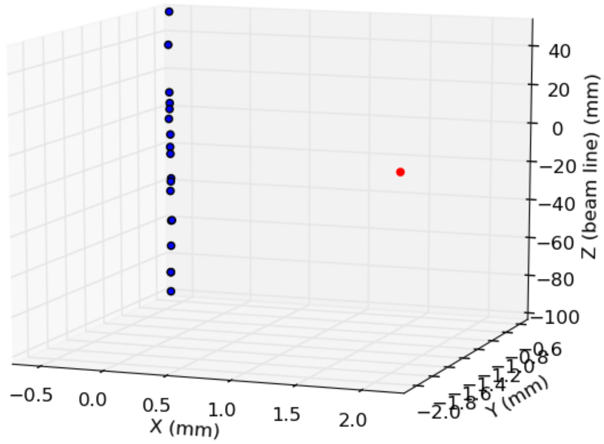

FIGURE 4.6: The dimuon decay vertex (red) is clearly distinguishable from the blue primary decay vertices (blue), which lie along the beam line.

fully reconstructing the b-hadron to determine the decay time distribution, the psuedo proper time, τ, will be used. τ is defined as

$$\tau = \frac{L_{xy} m_{J/\psi}}{p_T}, \tag{4.8}$$

where $L_{xy} = \vec{L} \cdot \vec{p_T}/p_T$, with $\vec{L}$ being the vector from the primary vertex to the dimuon decay vertex, and $\vec{p_T}$ is the transverse momentum vector of the dimuon system. $m_{J/\psi}$ is the mass of the J/ψ as given in the PDG [3]. Given that the b-hadron is not fully reconstructed, the J/ψ momentum is used as a proxy for the b-hadron momentum, and τ provides a good estimate of the b-hadron decay proper time [28]. L_{xy} can be used as a measurement of the displaced vertex in separating prompt and non-prompt decays, especially in the case where the p_T of the J/ψ aligns with that of the b-hadron. Although for a low p_T J/ψ the large opening angle between its flight direction and that of the b-hadron can affect the reliability of this method, Monte Carlo simulations have shown that a reliable fraction of non-promptly produced J/ψs can indeed be extracted [21]. In the case of more than one primary vertex being recorded for an event due to pileup, the primary vertex with the z-component closest to the z-component of the dimuon vertex was chosen. Figure 4.6 presents the vertices recorded for a single event, with all of the blue markers along the beam line having been recorded as primary vertices due to pileup. The effect of selecting the incorrect vertex has been shown to have negligible impact on the calculation of the non-prompt production fraction [28].

The data were divided into 12 bins of dimuon p_T between 8 and 40 GeV, and a plot of τ produced for each bin. The width of the bins increased with higher p_T due to fewer J/ψs occurring in the later bins, as can be seen in Figure 4.7. An unweighted two-dimensional

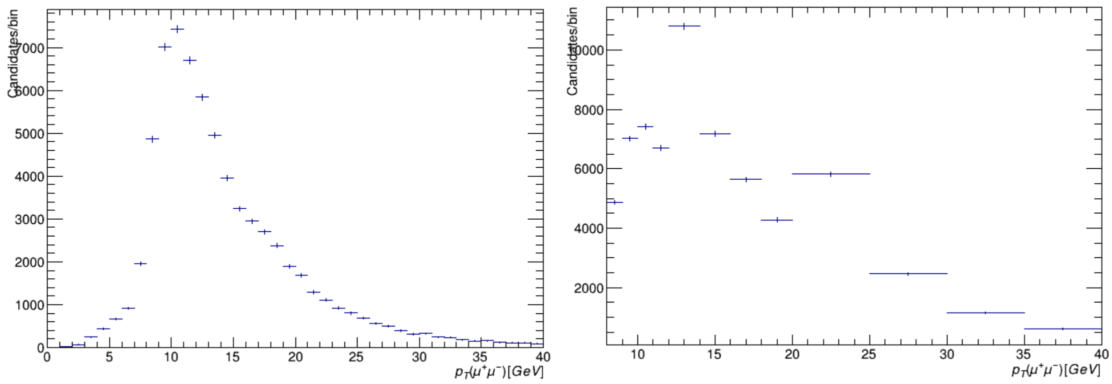

(A) p_T of the dimuon system

(B) p_T, rebinned as used in τ fit

FIGURE 4.7: Transverse momentum p_T of the dimuon spectrum

unbinned maximum likelihood fit to the data was used to distinguish prompt from non-prompt J/ψs, by fitting a convolution of three distributions to τ. Should the J/ψ be produced in a prompt process, $\tau = 0$ in principle (because $L_{xy} = 0$), and its distribution a δ-function. However, limited detector resolution suggests that the true distribution for the prompt J/ψs be a δ-function convoluted with a Gaussian distribution for a smearing effect. A non-prompt J/ψ will have $|\vec{L_{xy}}| > 0$, and hence $|\tau| > 0$. The behaviour of non-prompt contributions can be modelled by convolving a Guassian distribution centred at 0 with a single-sided decaying exponential [29]. This model allows for negative τ values. While a negative decay time is unphysical, it is possible to measure a negative τ due to limited detector resolution. This could occur when dot product in $L_{xy} = \vec{L} \cdot \vec{p_T}/p_T$ is negative, due to the possible mis-reconstruction of the decay vertices.

The background comes mainly from combinatorics of semi-leptonic b and c decays, as well as mis-reconstructed tracks of other hadrons decaying in flight [30]. Because these fake signatures can contribute both positive and negative τ, the background components were modelled with a simple double-sided decaying exponential.

Figure 4.8 is an example fit of the pseudo-proper time τ, and the complete set of fits in each p_T bin are displayed in Figures A.3 and A.4. The total fit is displayed in red, the prompt distribution is displayed in blue, the decaying exponential non-prompt distribution in purple, and the background in green. The simplified background model did not discriminate between prompt and non-prompt background components, and as a result the fit at the tails of the distribution can deviate from the data. However, the statistical significance of this deviation is small.

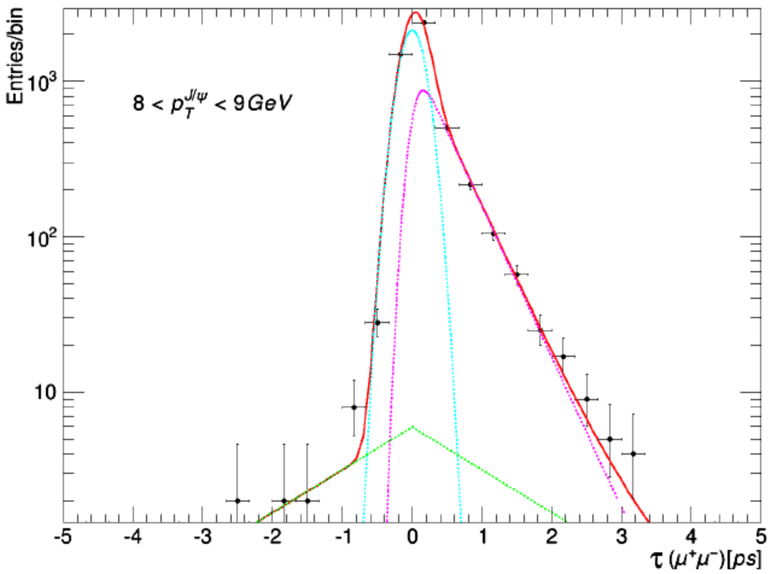

FIGURE 4.8: An example fit of the pseudo-proper time τ in the $8 < p_T < 9$ GeV bin.

The non-prompt J/ψ production fraction was used as a parameter in the fitting procedure, and is plotted in Figure 4.9(A) against p_T of the J/ψ. The horizontal bars represent the range of p_T for the bin, and the vertical error bars represent the statistical uncertainties in the fit. The fit is compared to a recent publication by ATLAS [30], shown in Figure 4.9(B). The non-prompt fraction is found in this analysis to increase with increasing p_T, from 0.39 for $8 < p_T < 9$ GeV to 0.68 for $35 < p_T < 40$ GeV. We see a deviation from the otherwise uniform increase of non-prompt fraction with increasing p_T at the bin with $14 < p_T < 16$ GeV. This could be due to the simplified model of the background, which could have led to an incorrect fractional fit.

The increase of the non-prompt J/ψ production fraction with increasing p_T indicates that the non-prompt cross section does not fall as rapidly with p_T as the prompt cross section. The prompt cross section is calculable using NLO and a partial NNLO perturbative QCD [25]. Figures A.1 and A.2 show the prompt and non-prompt cross sections of the J/ψ as a function of p_T, as measured by ATLAS at $\sqrt{s} = 7$ TeV [25], and their agreement with theoretical predications. We see that the theoretical predictions for both the prompt and non-prompt cross sections agree reasonably well, although there is discrepancy between data and theory at higher p_T. Comparing the plots, the differential cross section of the $B \rightarrow J/\psi$ process is predicted to be lower than that of prompt QCD processes at low p_T, leading to a low non-prompt production fraction [31]. As p_T increases, the prompt cross section falls off far more rapidly than the non-prompt cross section, giving rise to the increasing fraction of non-prompt J/ψ production at higher p_T.

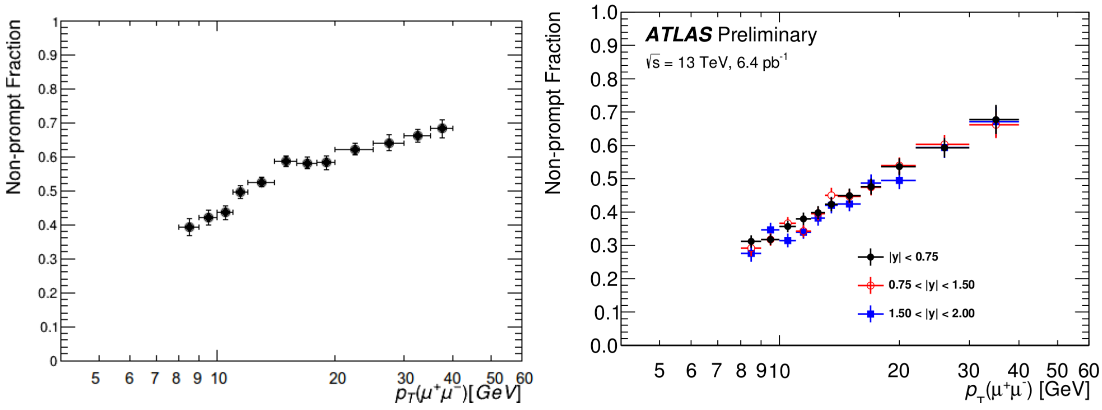

(A) (B)

FIGURE 4.9: The non-prompt J/ψ production fraction as measured in this analysis (A) compared to that as measured by ATLAS (B) [30].

The ATLAS plot displays the same increasing trend in non-prompt fraction as a function of p_T, although the low p_T fraction is lower than was measured here. This could again be due to an incorrect modelling of the background in this analysis, which led to a much smaller fraction of the data being interpreted as background than was done in the ATLAS analysis.

Chapter 5

Upsilon meson Υ

The Υ meson was discovered three years after the J/ψ, and is a $b\bar{b}$ quarkonium. Like the J/ψ, it is an S-wave (L=0) vector (S=1) $J^{PC} = 1^{--}$ state. It has a mass of (9460.30 $\pm$ 0.26) MeV [3], and a lifetime of 1.21×10^{-20}s. The $\Upsilon(nS)(n = 1, 2, 3)$ resonances live in a narrow vicinity, with masses of (10.02326 $\pm$ 0.00031) GeV and (10.3552 $\pm$ 0.0005) GeV [3] for $n = 2, 3$ respectively. The Υ decay to a muon pair ($\Upsilon \to \mu^+\mu^-$) has a branching fraction $\Gamma_i/\Gamma = (2.48 \pm 0.05)\%$ [3].

Like the prompt production of the J/ψ, Υ production can occur directly in the hard interaction (parton scattering), or via feed-down from heavier bottomonium states, like the χ_b or excited Υ states [23]. Because the Υ is a $b\bar{b}$ meson, it cannot be produced through the decay of a b-hadron as was done for the non-prompt J/ψ production. The only quark heavier than the b is the t, which decays too quickly to form hadrons due to its enormous mass, so the only decays which result in an Υ are heavier bottomonium states. The production of the Υ consists therefore of purely prompt processes.

Similarly to the production of the J/ψ, the Colour Evaporation Model, the Colour Singlet Model and the Colour Octet Model attempt with some success to describe the production of the Υ meson. The same successes and failings as discussed in relation to the J/ψ are applicable to Υ production.

As in the case of the J/ψ and η_c, a spin 0 $b\bar{b}$ state (the η_b meson) does exist, and decays again predominantly via hadrons, and so will not be discussed in this analysis.

5.1 Invariant Mass

The Υ is clearly present in the dimuon spectrum, as shown by Figure 5.1. There is a clear peak corresponding to the resonance of the $\Upsilon(1S)$, and a second peak due to interference between the $\Upsilon(2S/3S)$ states. Because the first two excited states are so close together, the peaks are not distinguishable here, and no attempt is made to extract their masses. The fit to the Υ invariant mass is shown by Figure 5.2, and yields a result of (9454 ± 18) MeV, in agreement with the PDG within 1σ.

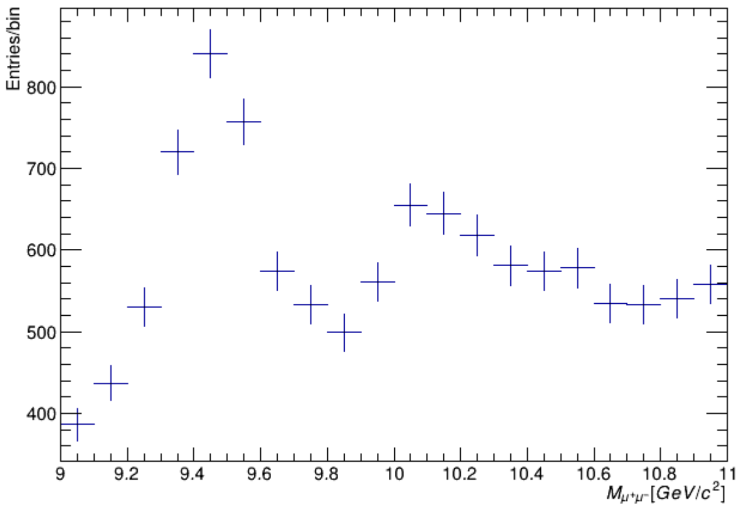

FIGURE 5.1: The dimuon invariant mass plot in the vicinity of the Υ resonance.

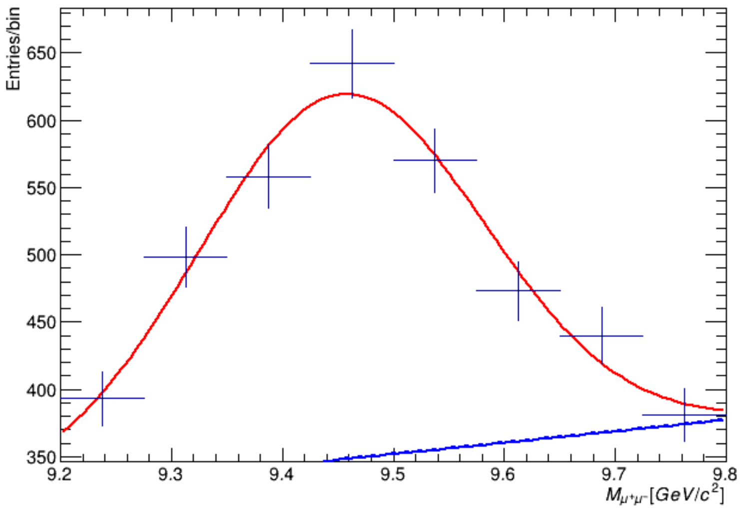

FIGURE 5.2: The fit to the Υ invariant mass, shown in red, was done using a Gaussian distribution to model the signal and a second degree polynomial to model the background (shown in blue), due to interference from the excited states $\Upsilon(2S/3S)$.

Chapter 6

Uncertainties

All uncertainties quoted throughout this analysis are purely statistical and are given by a χ^2 minimization method unless otherwise stated. There are several systematic uncertainties which have not been dealt with here which should contribute to the uncertainty in the results obtained. These could be dealt with in a more rigorous analysis.

6.1 Systematic Uncertainties in Invariant Mass Fits

• The systematics of detector calibrations were not accounted for. Finite detector resolution leads to a smearing of the distributions in each of the fits, leading to an increased uncertainty in the measurement.

• The final state muons undergo bremsstrahlung radiation, leading to them being observed and reconstructed at a lower energy. The partons also undergo initial state radiation, leading to a lower energy ($\hat{s}$) collision. Both of these effects lead to a lower invariant mass being reconstructed, and have not been dealt with here.

• The convolution of the proton PDFs, which lead to a mass peak which is lower than the expected value [3], have not been dealt with. This occurs because the PDFs increase at low x (the momentum fraction carried by the parton), so more of the partons carry a low fraction of the proton momentum. The initial state of the hard scatter is therefore likely to have a lower $\hat{s}$, which leads to a lower mass distribution of the particle produced in the collision.

• The impact of the fit parameters on the results could be considered using an alternative background model or a Crystal Ball function to fit the mass distribution.

6.2 Systematic Uncertainties in Calculating the Non-Prompt Fraction

• The tracking efficiency of the Inner Detector and the muon reconstruction efficiency is assumed to cancel in the calculation of the non-prompt production fraction [28], and so has not been considered.

• The main source of systematic uncertainty is introduced by the fit to the pseudo-proper time τ. The fit was done using an unbinned -Log(Likelihood) method where the minimization and error analysis is performed by MINUIT [32]. Additional sources of uncertainty have not been considered. In order to asses the uncertainty introduced by the fit, alternative models for the pseudo-proper time could be considered.

• Uncertainty is introduced through the simplified background modelling. A single double-sided decaying exponential was used for all 12 of the p_T bins, and there is thus some deviation of the fit from the data at the tail of the distributions. However, these data points have very little statistical significance in the totality of the fit. However, the magnitude of the background fit to the τ distribution is much less than that plotted in the latest ATLAS analyses [28], [30], which could lead to error in the calculation of the non-prompt fraction. Again, this could be examined by changing the models for the background distribution.

Chapter 7

Conclusions

The dimuon spectrum was examined in this paper, and several resonances were identified. The analysis was performed on proton-proton collisions from the LHC at a center of mass energy of 13 TeV, using (3.6 ± 0.2) fb^{-1} of data, collected in June 2015.

The invariant masses of the Z boson, J/ψ, $\psi(2S)$ and Υ(1S) were fitted and compared to values given by the Particle Data Group. The fits to data yielded results of (3094.5 ± 0.5) MeV and (3689 ± 4) MeV for the invariant masses of the J/ψ and $\psi(2S)$ mesons. The $\psi(2S)$ result agrees with the PDG within 1σ. The mass of the J/ψ disagrees by 5σ with the PDG. The mass of the Υ was found to be (9454 ± 18) MeV, agreeing within 1σ with the PDG. The mass of the Z was found to be (90.92 ± 0.09) GeV, which agrees within 3σ with the PDG. Both the J/ψ and Z masses are found here to have lower values than expected, for reasons discussed in the previous section.

The J/ψ invariant mass is quoted with a very small uncertainty, as its narrow width leads to a statistically good fit. However, the fit could be improved through the use of a Crystal Ball function, to include the low-mass tail. The invariant mass is shifted to a lower value due to the processes described above, including bremsstrahlung radiation and PDF convolution.

Models of prompt and non-prompt J/ψ production were discussed, and the non-prompt J/ψ were separated using a fit to the J/ψ pseudo-proper time. The non-prompt production fraction was found to increase with increasing p_T of the dimuon system, and agrees fairly well with published results by ATLAS [30]. Discrepancies are due to this analysis using a simplified model, including a generalised background function. The trend displayed by the results agree with theoretical predictions.

The dimuon spectrum is an important validation of our knowledge of how particles behave. In particular, measurements involving the J/ψ prompt and non-prompt production models are important probes into our theoretical understanding, and further studies at increasing $\sqrt{s}$ will continue to shed light on the puzzle of J/ψ production.

Appendix A

Appendix

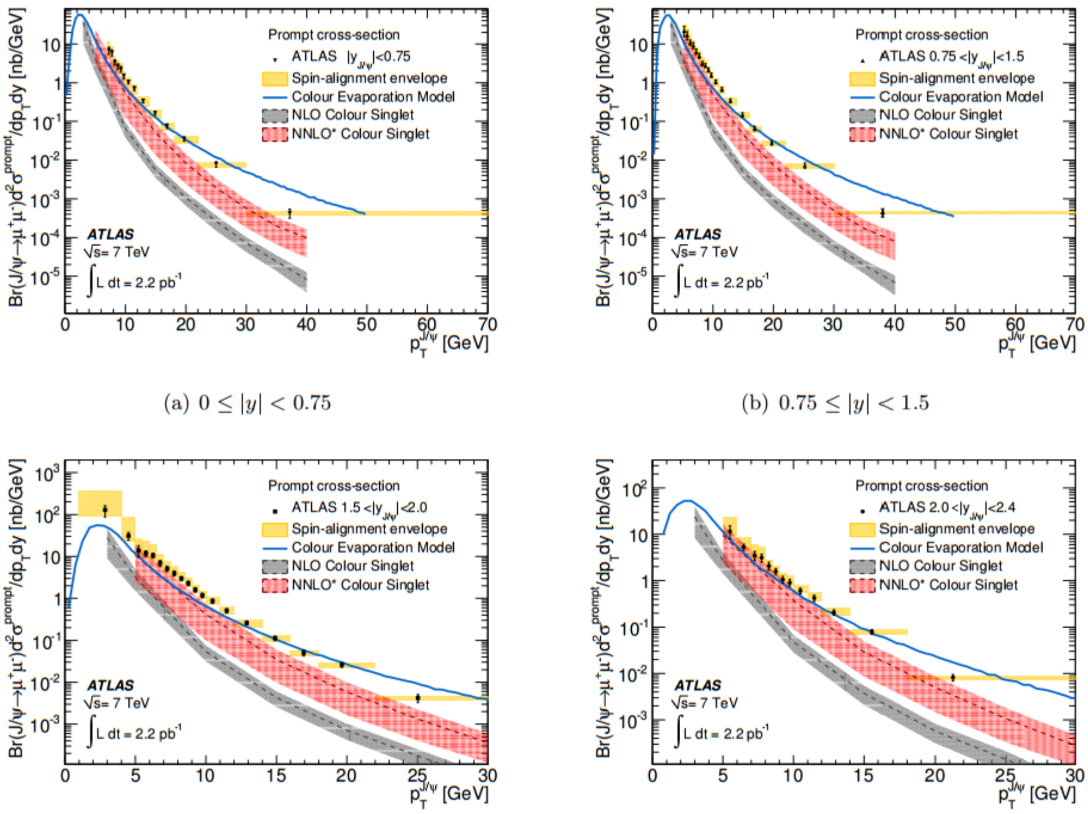

(a) $0 \leq |y| < 0.75$

(b) $0.75 \leq |y| < 1.5$

(c) $1.5 \leq |y| < 2$

(d) $1.5 \leq |y| < 2.4$

FIGURE A.1: The theoretical prompt cross-section due to the CEM, NLO CSM and NNLO CSM as compared to experimental data. The yellow bands represent the spin alignment uncertainty, and the red and grey bands represent the theoretical uncertainty [25]

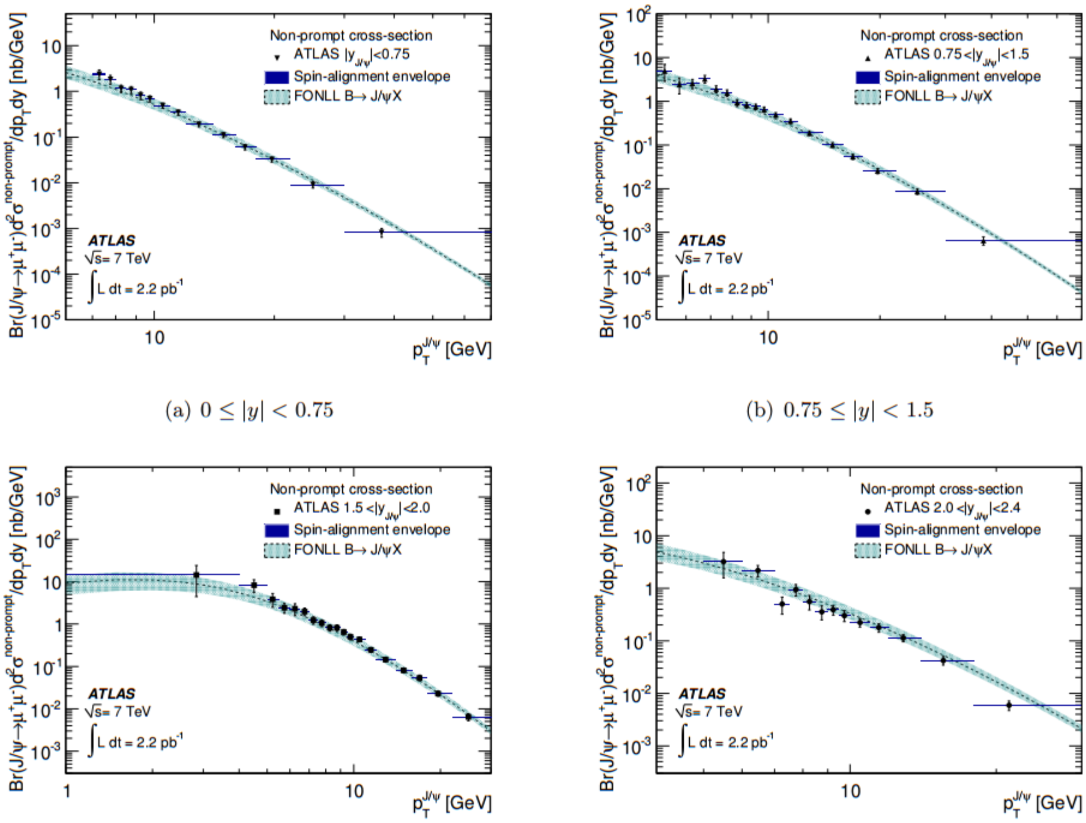

(a) $0 \leq |y| < 0.75$

(b) $0.75 \leq |y| < 1.5$

(c) $1.5 \leq |y| < 2$

(d) $1.5 \leq |y| < 2.4$

FIGURE A.2: Theoretical non-prompt cross-section calculation due to predictions by FONLL compared to experimental data. The dark blue bands represent the spin alignment uncertainty, and the light blue bands represent experimental uncertainty [25]

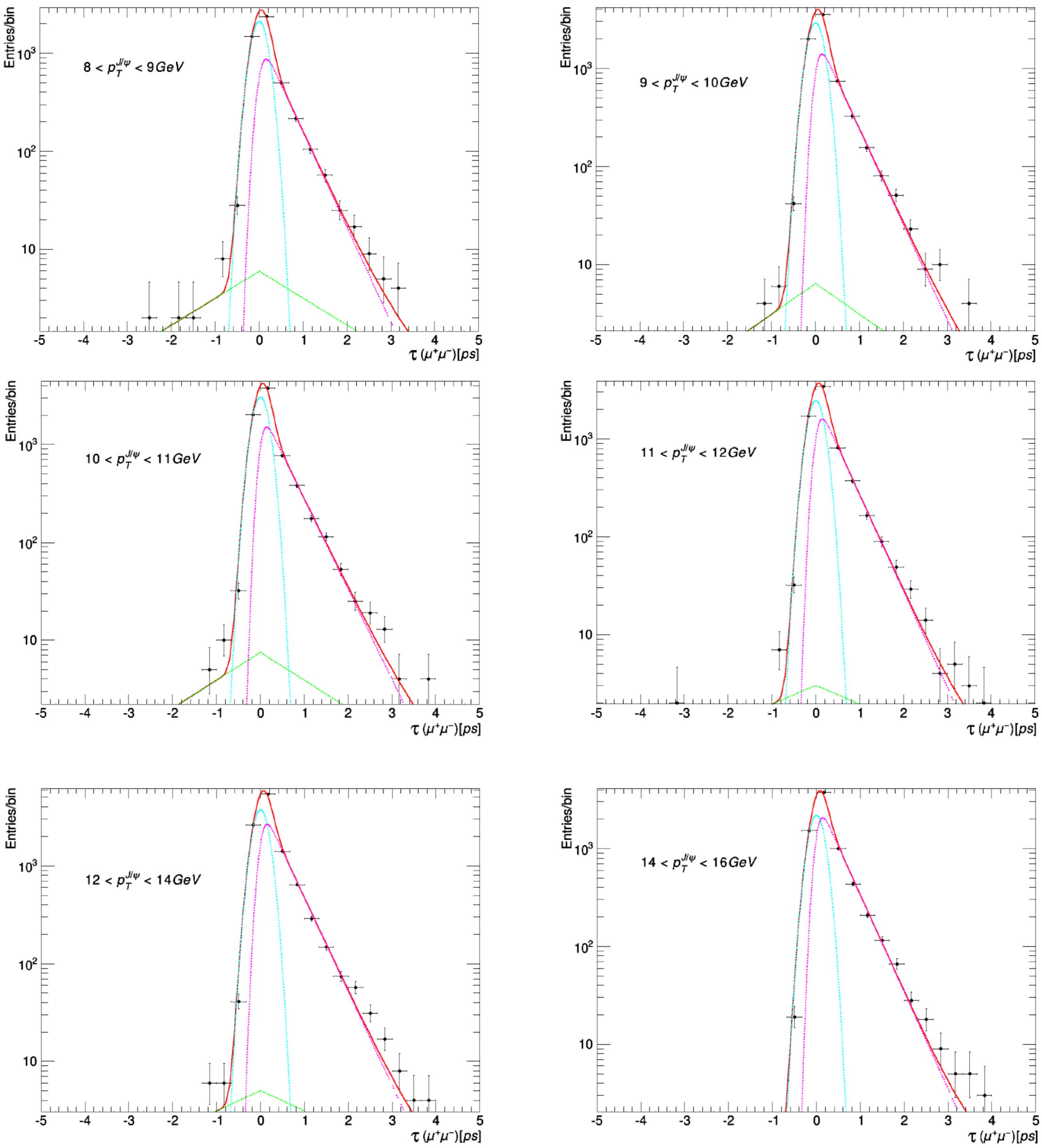

FIGURE A.3: Fitted plots of the pseudo-proper time τ in bins of p_T

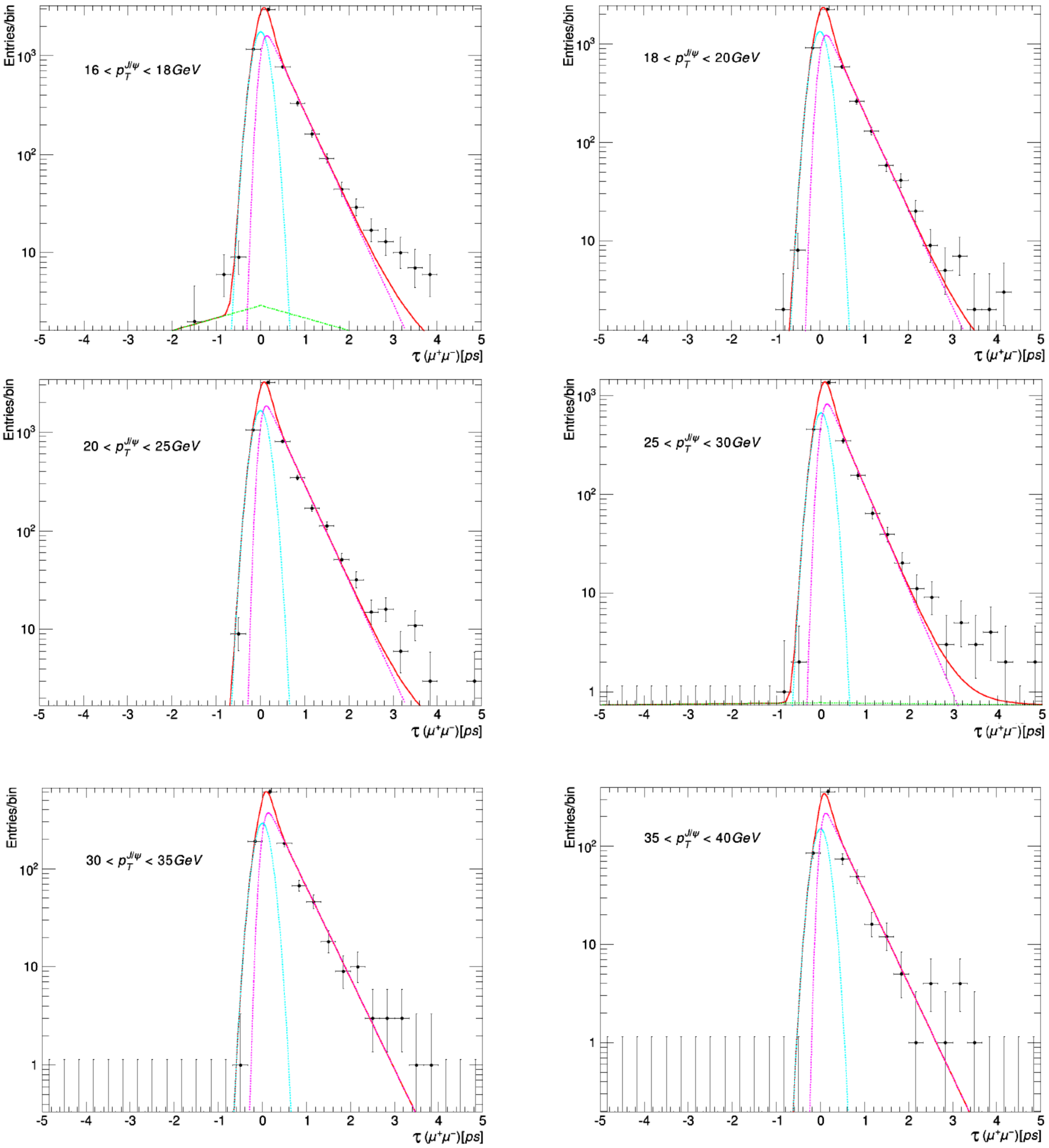

FIGURE A.4: Fitted plots (continued) of the pseudo-proper time τ in bins of p_T

Bibliography

[1] M. Thompson, *Modern Particle Physics.* Cambridge University Press, 2013.

[2] D. Griffiths, *Introduction to Elementary Particles.* WILEY VCH Verlag GmbH and Co. KGaA, 2008.

[3] **Particle Data Group** Collaboration, K. A. Olive *et al.*, "Review of Particle Physics," *Chin. Phys.* **C38** (2014) 090001.

[4] P. W. Higgs, "Broken symmetries and the masses of gauge bosons," *Phys. Rev. Lett.* **13** (Oct, 1964) 508–509. `http://link.aps.org/doi/10.1103/PhysRevLett.13.508`.

[5] **ATLAS** Collaboration, G. Aad *et al.*, "Observation of a new particle in the search for the Standard Model Higgs boson with the ATLAS detector at the LHC," *Phys. Lett.* **B716** (2012) 1–29, `arXiv:1207.7214 [hep-ex]`.

[6] **CMS** Collaboration, S. Chatrchyan *et al.*, "Observation of a new boson at a mass of 125 GeV with the CMS experiment at the LHC," *Phys. Lett.* **B716** (2013) 30–61, `arXiv:1207.7235 [hep-ex]`.

[7] M. Thomson, "Handout 8: Quantum chromodynamics," 2009.

[8] **LHCb** Collaboration, R. Aaij *et al.*, "Observation of J/ψ Resonances Consistent with Pentaquark States in ${\lambda_b}^0 \to J/\psi K^-$p Decays," *Phys. Rev. Lett.* **115** (2015) 072001, `arXiv:1507.03414 [hep-ex]`.

[9] K. Whalen, *From discovery to precision measurements: electron identification, electron-like backgrounds, and measurement of the differential fiducial cross-sections of the Higgs boson in the four-lepton decay channel with the ATLAS detector.* PhD thesis, 2015.

[10] A. D. Martin, W. J. Stirling, R. S. Thorne, and G. Watt, "Parton distributions for the LHC," *Eur. Phys. J.* **C63** (2009) 189–285, `arXiv:0901.0002 [hep-ph]`.

[11] G. Aad *et al.*, "The atlas experiment at the cern large hadron collider," *Journal of Instrumentation* **3** no. 08, (2008) S08003. `http://stacks.iop.org/1748-0221/3/i=08/a=S08003`.

[12] J. Pequenao and P. Schaffner, "An computer generated image representing how atlas detects particles." Jan, 2013.

[13] G. Artoni, G. Barone, K. M. Loew, H. Herde, G. Sciolla, M. Bellomo, M. Goblirsch-Kolb, N. M. Koehler, M. Sioli, R. Nicolaidou, A. Lesage, D. Zhang, S. Hu, S. Zambito, and F. Sforza, "Muon reconstruction performance in early run ii," Tech. Rep. ATL-COM-MUON-2015-037, CERN, Geneva, Jul, 2015. `https://cds.cern.ch/record/2039693`.

[14] L. M. Kashif, *Measurement of the Z boson cross-section in the dimuon channel in pp collisions at* $\sqrt{s} = 7$ *TeV*. PhD thesis, Harvard University, 2010.

[15] J. J. Aubert, U. Becker, P. J. Biggs, J. Burger, M. Chen, G. Everhart, P. Goldhagen, J. Leong, T. McCorriston, T. G. Rhoades, M. Rohde, S. C. C. Ting, S. L. Wu, and Y. Y. Lee, "Experimental observation of a heavy particle j," *Phys. Rev. Lett.* **33** (Dec, 1974) 1404–1406. `http://link.aps.org/doi/10.1103/PhysRevLett.33.1404`.

[16] **SLAC-SP-017** Collaboration, J. E. Augustin *et al.*, "Discovery of a Narrow Resonance in e+ e- Annihilation," *Phys. Rev. Lett.* **33** (1974) 1406–1408. [Adv. Exp. Phys.5,141(1976)].

[17] T. J. LeCompte, "Charmonium 1: Introduction and production models.".

[18] "B Hadron Lifetimes," Tech. Rep. SLAC-PUB-5671, Stanford Linear Accelerator Center, Stanford, October, 1991.

[19] V. Khoze, A. Martin, M. Ryskin, and S. W.J., "Inelastic J/ψ meson and Υ hadroproduction," *Eur. Phys. J.* **C39** (2005) 163–171.

[20] M. Kramer, "Color-Singlet and Color-Octet Contributions to J/ψ Photoproduction," *http://arxiv.org/pdf/hep-ph/9609416v1.pdf* (1996) .

[21] **CDF** Collaboration, D. Acosta *et al.*, "Measurement of the J/ψ meson and $b-$hadron production cross sections in $p\bar{p}$ collisions at $\sqrt{s} = 1960$ GeV," *Phys. Rev.* **D71** (2005) 032001.

[22] **CDF** Collaboration, F. Abe *et al.*, "J/ψ and $\psi(2S)$ Production in $p\bar{p}$ collisions at $\sqrt{s} = 1.8$ TeV," *Physical Review Letters* **79-4** (1997) 572–577.

[23] **LHCb** Collaboration, R. Aaij *et al.*, "Measurement of Υ production in pp collisions at $\sqrt{s} = 2.76$ TeV," hep-ex/1402.2539v2.

[24] M. Cacciari, "Hadronic production of heavy quarks," arXiv:hep-ph/9710527 [hep-ph]. [AIP Conf. Proc.424,189(1998)].

[25] A. Nelson, *Measurement of the differential cross-section with respect to momentum and rapidity of the J/ψ meson and the non-prompt J/ψ cross-section fraction in pp collisions at $\sqrt{s} = 7$ TeV with the ATLAS detector.* PhD thesis, 2011.

[26] M. Cacciari, F. Stefano, and P. Nason, "The p_T spectrum in heavy-flavour photoproduction," arXiv:hep-ph/0102134v1 [hep-ph].

[27] M. Cacciari, M. Greco, and P. Nason, "The p_T spectrum in heavy-flavour hadroproduction," arXiv:hep-ph/9803400v1 [hep-ph].

[28] "Measurement of the differential cross-sections of prompt and non-prompt production of J/ψ and ψ(2S) in pp collisions at $\sqrt{s} = 7$ and 8TeV with the ATLAS detector," Tech. Rep. ATLAS-CONF-2015-024, CERN, Geneva, Jul, 2015. https://cds.cern.ch/record/2031453.

[29] C. Maiani, *Studies of the Di-Muon Resonances at the ATLAS Experiment at CERN.* PhD thesis, Università di Roma 'La Sapienza'.

[30] "Measurement of the differential non-prompt J/ψ production fraction in $\sqrt{s} = 13$ TeV pp collisions at the ATLAS experiment," Tech. Rep. ATLAS-CONF-2015-030, CERN, Geneva, Jul, 2015. http://cds.cern.ch/record/2037967.

[31] **CMS Collaboration** Collaboration, V. Khachatryan *et al.*, "Prompt and non-prompt J/ψ production in pp collisions at $\sqrt{s} = 7$ TeV," *Eur. Phys. J. C* **71** no. arXiv:1011.4193. CERN-PH-EP-2010-046. CMS-BPH-10-002, (Nov, 2010) 1575. 38 p. http://cds.cern.ch/record/1308135.

[32] W. Verkerke and D. Kirkby, *RooFit Users Manual.* CERN.